Research Article

Received: 2 June 2020 Revised: 9 July 2020 Accepted article published: 20 July 2020 Published online in Wiley Online Library:

(wileyonlinelibrary.com) DOI 10.1002/pi.6088

Phosphonium-based polythiophene conjugated polyelectrolytes with different surfactant counterions: thermal properties, self-assembly and photovoltaic performances

Michèle Chevrier,[a,b] Jurgen Kesters,[c] Judith E. Houston,[d] Niko Van den Brande,[e] Sylvain Chambon,[f] Sébastien Richeter,[a] Bruno Van Mele,[e] Thomas Arnold,[g,h,i,j] Ahmad Mehdi,[a] Roberto Lazzaroni,[k] Philippe Dubois,[b] Rachel C. Evans,[l] Wouter Maes[c] and Sébastien Clément[a*]

Abstract

Phosphonium-based polythiophene conjugated polyelectrolytes (CPEs) with three different counterions (dodecylsulfate, octylsulfate and perfluorooctane sulfonate) are synthesized to determine how the nature of the counterion affects the thermal properties, the self-assembly in thin films and the performance as the cathode interfacial layer in polymer solar cells (PSCs). The counterion has a significant effect on the thermal properties of the CPEs, affecting both their glass transition and crystalline behaviour. Grazing-incidence wide-angle X-ray scattering studies also indicate that changing the nature of the counterion influences the microstructural organization in thin films (face-on *versus* edge-on orientation). The affinity of the CPEs with the underlying photoactive layer in PSCs is highly correlated with the counterion species. Finally, in addition to an increase of the power conversion efficiency of *ca* 15% when using these CPEs as cathode interfacial layers in PSCs, a higher device stability is noted, compared to a reference device with a calcium interlayer.

Supporting information may be found in the online version of this article.

Keywords: conjugated polyelectrolytes; surfactant counteranion; self-assembly; thin films; cathode interlayers; organic solar cells

* *Correspondence to: S Clément: ICGM, Univ. Montpellier, CNRS, ENSCM, Montpellier, France. E-mail: sebastien.clement1@umontpellier.fr*

a *ICGM, Univ. Montpellier, CNRS, ENSCM, Montpellier, France*

b *Service des Matériaux Polymères et Composites (SMPC), Centre d'Innovation et de Recherche en Matériaux et Polymères (CIRMAP), Université de Mons – UMONS, Mons, Belgium*

c *UHasselt – Hasselt University, Institute for Materials Research (IMO), Design and Synthesis of Organic Semiconductors (DSOS), Diepenbeek, Belgium*

d *Jülich Centre for Neutron Science (JCNS) at the Heinz Maier-Leibnitz Zentrum (MLZ), Forschungszentrum Jülich GmbH, Garching, Germany*

e *Physical Chemistry and Polymer Science (FYSC), Vrije Universiteit Brussel (VUB), Brussels, Belgium*

f *Univ. Bordeaux, IMS, CNRS, UMR 5218, Bordeaux INP, ENSCBP, Talence, France*

g *Diamond Light Source Ltd, Harwell Science and Innovation Campus, Didcot, UK*

h *European Spallation Source ERIC, Lund, Sweden*

i *Department of Chemistry, University of Bath, Bath, UK*

j *ISIS Neutron and Muon Source, Rutherford Appleton Laboratory, Didcot, UK*

k *Laboratory for Chemistry of Novel Materials, CIRMAP, University of Mons – UMONS, Mons, Belgium*

l *Department of Materials Science and Metallurgy, University of Cambridge, Cambridge, UK*

INTRODUCTION

Conjugated polyelectrolytes (CPEs) are polymers with a π-delocalized backbone bearing ionic side chain groups.[1] CPEs combine the physicochemical properties of polyelectrolytes, which are dependent on complex long-range electrostatic interactions, with the optical and electronic properties of organic semiconducting polymers, which are closely linked to the chain conformation and interchain interactions.[1] The presence of pendant substituents with ionic functionalities allows their dissolution in highly polar solvents, including water, and their interaction with other ionic species such as metal ions, molecular ions, polyelectrolytes, proteins and DNA through electrostatic interactions.[2,3] Thus, combining the intrinsic light-harvesting properties of the conjugated polymer backbone with the solubility in aqueous media has opened the door to the use of these materials as optical platforms for the detection of biological targets with increased sensitivity compared to small molecules.[4–7] Besides chemosensing and biosensing, CPEs also show great potential for application in organic optoelectronic devices such as light-emitting diodes,[8–13]organic electrochemical transistors[14–18] and organic photovoltaic devices.[12,13,19,20] Indeed, their solubility in highly polar solvents offers the opportunity to fabricate multilayer devices without interface mixing by depositing different layers from orthogonal solvents.[13,20,21] In addition, the presence of the ionic side groups has been found to induce the formation of an interfacial dipole, leading to a reduced work function (W_F) of the metal electrodes and thus improved charge collection and performance.[22–25]

Optoelectronic devices are generally fabricated through solution processing. Due to their inherent amphiphilic nature, CPEs tend to self-assemble into aggregates with a conducting core (hydrophobic conjugated backbone) and an insulating shell (hydrophilic ionic pendent groups) which nucleate and drive the film morphology.[26–28] As such, large insulating domains between conduction pathways (i.e. $\pi-\pi$ interactions) are expected from this self-assembly, which are detrimental for device performance. Since the device performance depends both on the intrinsically linked optoelectronic properties and the nanoscale morphology of the polymer,[29,30] determining the parameters influencing the CPE thin film morphology and its interdependent optoelectronic properties is paramount for achieving high-performance organic optoelectronic devices.

Among the structural parameters that might affect the self-assembly and the optoelectronic properties, the nature of the charge-compensating counterions has been identified as a possible lever to control such properties.[31–33] Indeed, McCullough *et al.* have observed the strong dependence of the absorption spectra of polythiophene-based CPEs on the counterion nature, in particular its size.[34] Larger counterions prevent polyionic main chains from getting into contact with each other by increasing the average interchain distance, which reduces aggregation of polyions and fluorescence self-quenching.[31–33,35] Similarly, the exchange of the native counterion by an ionic surfactant has also been proved to break up CPE aggregates, leading to the formation of well-organized structures across multiple length scales.[27,36–42] The type of charge-compensating counterions can also significantly influence the electronic properties of CPEs.[32,35,43,44] Cao and coworkers have described how the type of counterion species can fine-tune the self-doping behaviour of n-type CPEs as well as the charge transport.[35] In addition, the properties of the interfaces in organic electronic devices can be fine-tuned by changing the type of counteranions in CPEs deposited on the electrode, generally leading to a decrease of the W_F of the electrodes, improved charge extraction and orders of magnitude changes in device performance.[35,45,46]

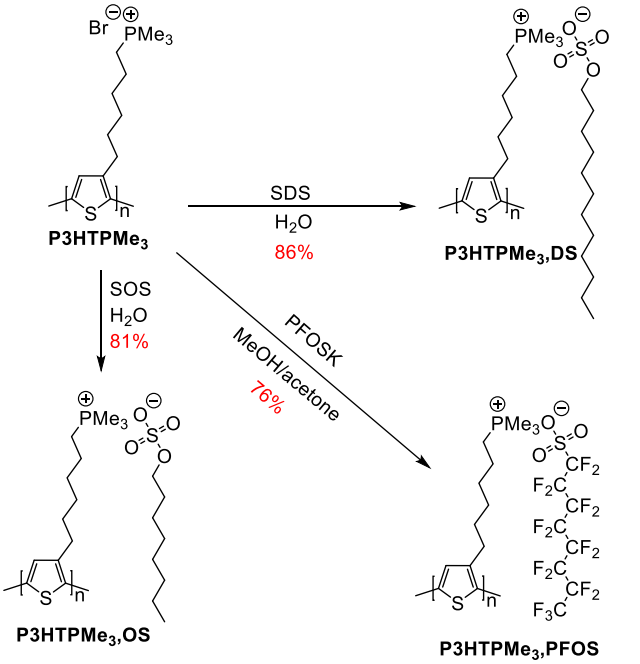

Scheme 1. Conversion of **P3HTPMe$_3$** into the corresponding **P3HTPMe$_3$,X** (X is OS, DS and PFOS) CPEs.

Herein, we examine a series of phosphonium-based polythiophenes incorporating a variety of charge-compensating counterions (X^-), namely dodecyl sulfate (DS), octyl sulfate (OS) and perfluorooctanesulfonate (PFOS) (**P3HTPMe$_3$,X**, Scheme 1). The study of their thermal properties reveals different degrees of crystallinity depending on the nature of the counterion. The self-assembly of the different CPEs in thin films is also investigated using grazing-incidence wide-angle X-ray scattering (GIWAXS). Cationic polythiophene-based CPEs have been found to be interesting materials for interfacial engineering in polymer solar cells (PSCs) enabling improved charge extraction and thus, power conversion efficiency (PCE).[19,21,47–49] Based on these results, the performance and the device stability in air of PSCs incorporating this series of CPEs with different counterions as cathodic interfacial layers have been determined.

MATERIALS AND METHODS

Materials

All reactions were carried out under argon using standard high vacuum and Schlenk techniques. Dry tetrahydrofuran was obtained by the solvent purification system PureSolve MD5 from Innovative Technology (Oldham, UK). Perfluorooctanesulfonic acid potassium salt (PFOSK) (98%) and sodium octyl sulfate (SOS) (95%) were purchased from Sigma Aldrich (Saint Quentin, France) and used as received. **P3HTPMe$_3$** and **P3HTPMe$_3$,DS** were prepared according to previously reported procedures.[21,50]

Characterization methods

^{1}H, ^{13}C{^{1}H}, ^{31}P{^{1}H} and ^{19}F Nuclear Magnetic Resonance (NMR) spectra were acquired with Bruker Avance 300 MHz and 600 MHz

spectrometers (Billerica, Massachusetts, USA), using the solvent as the chemical shift standard. All chemical shifts and coupling constants are reported in parts per million and hertz, respectively.

Number-averaged (M_n) and weight-averaged (M_w) molecular weights and the molecular weight distribution ($Đ$) of **P3HTBr** were measured using Size Exclusion Chromatography (SEC) on a Polymer Laboratories (PL) (Church Stretton, UK) liquid chromatograph equipped with a PL-DG802 degasser, an isocratic HPLC pump LC 1120 (flow rate of 1 mL min^{-1}), a Marathon autosampler (loop volume of 200 mL, solution concentration of 1 mg mL^{-1}), a PL-DRI refractive index detector and three columns: a PL gel 10 mm guard column and two PL gel Mixed-B 10 mm columns (linear columns for the separation of molecular weight polystyrene standards ranging from 500 to 10^6 Da). The eluent used was tetrahydrofuran at a flow rate of 1 mL min^{-1} at 35 °C. Polystyrene standards were used to calibrate the size exclusion chromatograph. X-ray Photoelectron Spectroscopy (XPS) analyses were performed using an Omicron Argus X-ray photoelectron spectrometer (Scienta Omicron, Germany) with a monochromated Al K_α radiation source ($h\nu$ = 1486.6 eV) with a 300 W electron beam power. The emission of photoelectrons from the sample was analysed at a takeoff angle of 90° under ultra-high vacuum conditions (≤10^{-10} Torr). The spectra were obtained with 100 eV pass energy for the survey scan and 20 eV pass energy for the F1s, C1s, O1s, N1s, S2p and P2p regions. All binding energies were calibrated against the C1s peak at 284.6 eV. The element peak intensities were corrected by Scofield factors.[51,52] The peak areas were determined after subtraction of a linear background. The spectra were fitted using Casa XPS v.2.3.15 software (Casa Software Ltd, UK) and applying a Gaussian/Lorentzian ratio *G/L* equal to 70/30.[51]

The electrochemical measurements were performed with an EcoChemie Autolab PGSTAT 30 potentiostat (Metrohm Autolab, Switzerland) using a three-electrode microcell with a platinum wire working electrode, a platinum wire counter electrode and an anhydrous $Ag/AgNO_3$ reference electrode (Ag/0.1 mol L^{-1} NBu_4PF_6 in MeCN containing 0.01 mol L^{-1} $AgNO_3$). The CPEs were analysed in solution in anhydrous acetonitrile containing 0.1 mol L^{-1} NBu_4PF_6. The electrolyte solution was degassed with Ar prior to each measurement. To prevent air from entering the system, a curtain of Ar was maintained during the differential pulse voltammetry experiments. For the conversion of volts to electronvolts, the onset potentials of the first oxidation/reduction peaks were used and referenced to ferrocene/ferrocenium, which has an ionization potential of −4.98 eV *versus* vacuum. This correction factor is based on a value of 0.31 eV for Fc/Fc^+ *versus* saturated calomel electrode[53] and a value of 4.68 eV for saturated calomel electrode *versus* vacuum:[54] $E_{HOMO/LUMO}$ (eV) = −4.98 − $E_{onset\ ox/red}^{Ag/AgNO3}$ (V) + $E_{onset\ Fc/Fc+}^{Ag/AgNO3}$ (V).

Thermal analyses were performed using a TA Instruments (New Castle, Delaware, USA) rapid heat-cool calorimeter equipped with liquid nitrogen cooling and specifically designed for operation at high scanning rate.[55] Helium (10 mL min^{-1}) was used as a purge gas. Before each experiment, the thermal history of the materials was erased by an initial heating cycle, ensuring the reproducibility of the observed transitions. It is worthwhile to mention that no solvent effects were seen in this initial heating, with the exception of a slight effect for **P3HTPMe$_3$,PFOS**, most probably caused by the presence of some residual solvent due to the preparation method. The measurements were performed by cooling at 500 K min^{-1} or 20 K min^{-1}, followed by heating at 500 K min^{-1} used for data interpretation.

Atomic Force Microscopy (AFM) measurements were performed using an Asylum Research MFP-3D™ instrument (Oxford instruments, UK) mounted on an anti-vibration plinth, in the tapping mode at room temperature under ambient conditions. Higher resolution AFM measurements were performed using diamond tips on silicon cantilevers, which were a kind gift from Adama Innovations (Ireland). The silicon cantilevers had a spring constant of *ca* 110 nN nm^{-1} and resonance frequency of *ca* 240 kHz. All raw AFM images were analysed using the Gwyddion 2.31 software (Czech Metrology Institute, Czech Republic).

Contact potential difference was determined using a Kelvin probe set-up from Besocke Delta Phi (Germany). A methanol solution containing the CPE (C = 1 mg mL^{-1}) was prepared in a nitrogen-filled glove box and stirred at room temperature for 24 h. Indium tin oxide (ITO) coated glass was cleaned using successive baths of Hellmanex, deionized water and isopropanol under sonication. 80 nm of silver (Ag) was deposited on ITO coated glass by thermal evaporation under high vacuum (P = 2 × 10^{-6} mbar). The CPE was deposited on the electrode (ITO and Ag) by spin-coating at 1000 rpm for 60 s. The contact potential difference of the different samples was measured subsequently and the work function (W_F) was estimated using freshly cleaved highly ordered pyrolytic graphite as a reference (4.65 eV).

GIWAXS measurements were performed on beamline I07, Diamond Light Source, UK.[56] The X-ray beam energy was E = 10 keV (wavelength λ = 1.24 Å) and the beam size was *ca* 100 × 200 μm ($v \times h$, full-width half-maximum, FWHM) with an approximately Gaussian intensity profile. An incident angle of α_i = 0.4° (>2 × α_c, the critical angle) was used, as this allows for complete illumination of the films with minimal substrate-reflected beam which could complicate analysis. The data were collected on a Pilatus P2M detector (DECTRIS) using a sample-to-detector distance of *ca* 237 mm, calibrated with silver behenate, giving an angular coverage of *ca* 30° and a q range of 0.1–3.5 $Å^{-1}$. **P3HTPMe$_3$,X** samples for GIWAXS were prepared by mixing 10 mg mL^{-1} solution of **P3HTPMe$_3$** with 10 mg mL^{-1} solution of surfactant to obtain the desired 1:1 charge ratio, with a total concentration of 10 mg mL^{-1}. The compositions of the **P3HTPMe$_3$**–surfactant mixtures are given in the ESI (Table S2). Solutions of **P3HTPMe$_3$,X** CPEs mixed with different counterions were spin-coated onto silicon wafers from 10 mg mL^{-1} methanolic solutions, resulting in films that were 70–80 nm thick. The samples were enclosed in a helium-filled chamber to reduce beam damage and background scattering and mounted on a hexapod to allow alignment. A fast shutter prevented unintended exposure to X-rays with extremely short exposure times of 1 s. The data were reduced using the data reduction and analysis software Data Analysis WorkbeNch (DAWN) and beamline scripts.[57] DAWN was also used to identify peak positions and widths, which have been directly related to the morphology.

Organic photovoltaic device fabrication and characterization

Bulk heterojunction (BHJ) PSCs were fabricated using the traditional architecture glass/ITO/PEDOT:PSS/PCDTBT:$PC_{71}BM$/**P3HTPMe$_3$,X** (or Ca)/Al. The PCDTBT donor polymer (M_n = 79 kDa, $Đ$ = 2.4) and $PC_{71}BM$ were obtained from SolarisChem (Québec, Canada) and Solenne (Groningen, Netherlands), respectively. Prior to processing, the ITO (Kintec, 100 nm, 20 Ω sq^{-1}) coated glass substrates were thoroughly cleaned using soap, demineralized water, acetone, isopropanol and a UV/O_3 treatment. PEDOT:PSS (poly(3,4-ethylenedioxythiophene):poly(styrenesulfonic acid)) (Heraeus

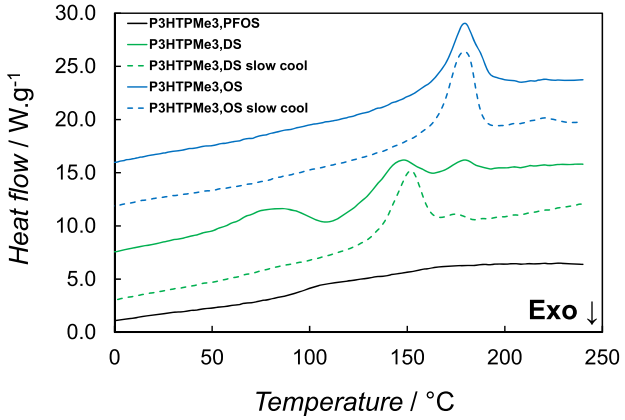

Figure 1. RHC thermograms of the **P3HTPMe$_3$,X** materials at 500 K min^{-1} heating rate, obtained after a previous cooling step at 500 K min^{-1} (solid lines) or 20 K min^{-1} (dashed lines). The curves are shifted vertically for clarity.

Clevios (Hanau, Germany)) was then deposited via spin-coating to obtain a layer thickness of *ca* 30 nm. Further processing was continued in a nitrogen-filled glovebox (O_2/H_2O < 0.1 ppm), initiated by thermal treatment for 15 min at 130 °C to remove any residual water. The photoactive layer blend PCDTBT:$PC_{71}BM$ was then spin-coated in a 1:4 ratio with a total concentration of 20 mg mL^{-1} from an *ortho*-dichlorobenzene solution. For the reference device without the CPE interlayer, Ca and Al electrodes were deposited with a thickness of *ca* 30 and *ca* 80 nm, respectively. For devices employing the interlayer materials, the CPEs were spin-coated from methanol as a processing solvent in different concentrations (0.25, 0.5 and 1 mg mL^{-1}) to optimize the solar cell parameters. Device fabrication was then completed by the deposition of an Al layer as the top electrode. The *J–V* characteristics were measured using a Newport class A solar simulator (model 91195A) (MKS Instruments, Inc., Andover, Massachusetts, USA) calibrated with a silicon solar cell to give an AM 1.5G spectrum. All data shown in this work are average values over four to eight cells. For the stability measurements, new devices were prepared with the optimized CPE concentrations and these solar cells were subjected to ambient air (in the dark) for 40, 80 and 120 min. *J–V* measurements were subsequently performed in a nitrogen atmosphere. AFM experiments on the solar cell devices were performed with a JPK NanoWizard 3 AFM (JPK Instruments AG, Berlin, Germany) using AC mode in air. Silicon ACTA-50 tips from AppNano with cantilever length *ca* 125 mm, spring constant *ca* 40 N m^{-1} and a resonance frequency *ca* 300 kHz were used. The scan angle, set point height, gain values and scan rate were adjusted according to the calibration of the AFM tip.

Polymer synthesis

General procedure for bromide counterion exchange by octyl sulfate (OS)

P3HTPMe$_3$ (0.100 g, 0.31 mmol) was dissolved in demineralized water (20 mL) and a solution of SOS (0.720 g, 3.11 mmol) in demineralized water (10 mL) was added dropwise. The solution was stirred at room temperature overnight and then poured into acetone (600 mL). The resultant black solid was filtered off, washed with acetone and dried under vacuum. Yield 81% (0.140 g).

^{1}H NMR (CD_3OD): δ = 0.90 (t, CH_3, 3H, $^3J_{H-H}$ = 7.0 Hz), 1.25–1.36 (m, 8H), 1.36–1.44 (m, 2H), 1.52–1.73 (m, 10H), 1.74–1.84 (m, 2H), 1.90 (d, 9H, $(CH_3)P$, $^2J_{P-H}$ = 14.5 Hz), 2.22–2.34 (m, 2H), 2.92 (br. t, 2H, $^3J_{H-H}$ = 7.8 Hz), 3.99 (t, 2H, CH_2–O–SO_3, $^3J_{H-H}$ = 6.6 Hz), 7.14 (s, 1H, Th) ppm. $^{13}C\{^1H\}$ NMR (CD_3OD): δ = 8.8 (d, $^1J_{P-C}$ = 55.0 Hz), 15.4, 23.3, 24.6, 24.8, 25.1, 30.8, 31.3, 31.4, 32.3, 32.4, 32.5, 33.9, 69.9, 131.1, 132.6, 135.8, 142.3 ppm. $^{31}P\{^1H\}$ NMR (CD_3OD): δ = 27.2 ppm. UV–visible (MeOH): λ_{max} = 445 nm.

General procedure for bromide counterion exchange by perfluorooctanesulfonate (PFOS)

P3HTPMe$_3$ (0.100 g, 0.31 mmol) was dissolved in methanol (20 mL) and a solution of PFOSK (1.000 g, 1.86 mmol) in a 1:1 methanol/acetone mixture (20 mL) was added dropwise. The solution was stirred at room temperature overnight and then poured into diethyl ether (600 mL) to precipitate the polymer. After filtration, the residue was suspended in water (500 mL) and stirred at 50 °C for 24 h to remove the excess of PFOSK. The polymer was then isolated by filtration, washed with water (3 × 30 mL) and diethyl ether (3 × 30 mL) and dried under vacuum, leading to a red solid. Yield: 76% (0.229 g).

^{1}H NMR (acetone-d_6): δ = 1.55–1.63 (m, 4H), 1.74–1.81 (m, 4H), 2.03 (d, 9H, $(CH_3)P$, $^2J_{P-H}$ = 14.7 Hz), 2.42–2.48 (m, 2H), 2.92 (br. t, 2H, $^3J_{H-H}$ = 7.8 Hz), 7.23 (s, 1H, Th) ppm. ^{19}F NMR (acetone-d_6): δ = −72.6, −81.7, −115.1, −120.9, −122.7, −123.2, −126.7 ppm. $^{31}P\{^1H\}$ NMR (acetone-d_6): δ = 27.7 ppm. UV–visible (MeOH): λ_{max} = 447 nm.

RESULTS AND DISCUSSION

Polymer synthesis and characterization

The phosphonium-substituted polythiophene polyelectrolyte starting material was synthesized according to a previously reported procedure.[50] Briefly, Kumada catalyst-transfer condensative polymerization was first used to generate the neutral bromohexyl-functionalized precursor, **P3HTBr** (M_n = 13 600 g mol^{-1}, $Đ$ = 1.36). Post-polymerization reaction with trimethylphosphine introduced the phosphonium cationic moiety, yielding **P3HTPMe$_3$**. As a final modification, the counterion exchange was carried out by adding an excess of salt from the counterion of interest into a **P3HTPMe$_3$** solution while vigorously stirring (Scheme 1).

After precipitation, the resulting solid was filtered off on a cellulose membrane and washed and dried *in vacuo* affording **P3HTPMe$_3$,X** (where X is OS, DS[21] or PFOS). All P3HTPMe$_3$,X CPEs were characterized by multinuclear NMR spectroscopy (Fig. S1-S6). Ion exchange was confirmed by ^{1}H NMR spectroscopy and XPS. The signals at 2.92 and 3.99 ppm in the ^{1}H NMR spectrum of **P3HTPMe$_3$,OS**, assigned to the methylene groups linked to the thiophene ring and the methylene groups adjacent to the sulfate in the OS anion, respectively, allowed the molar ratio between the cationic polythiophene and the OS anionic moieties to be determined (Fig. S1). By integrating these two signals, the molar ratio between **P3HTPMe$_3$** and OS was found to be very close to 1:1, as expected. The presence of the PFOS counterion in the **P3HTPMe$_3$,PFOS** CPE was evidenced using ^{19}F NMR spectroscopy, where signals at −72.6, −81.7 and between −115 and −127 ppm were observed (Fig. S5). In the XPS spectra of the CPEs following the exchange of Br^- with different anions (Figs S7–S9), the Br3d peak at 68 eV was no longer observed, indicating that the counterion exchange occurred quantitatively. The frontier orbital energy levels of the three **P3HTPMe$_3$,X** were determined by differential pulse voltammetry. The onset oxidation potentials were estimated to be 0.12, 0.27 and 0.30 V (*versus* Fc/Fc^+) for **P3HTPMe$_3$,DS**, **P3HTPMe$_3$,PFOS** and **P3HTPMe$_3$,OS**,

respectively. From these values, the highest occupied molecular orbital (HOMO) energy levels were calculated as −5.01, −5.17 and −5.20 eV for **P3HTPMe$_3$,DS**, **P3HTPMe$_3$,PFOS** and **P3HTPMe$_3$,OS**, respectively (Table S1). Similarly, the nature of the counterions also had little effect on the lowest unoccupied molecular orbital (LUMO) energy levels with values of −2.99, −2.98 and −2.96 eV for **P3HTPMe$_3$,DS**, **P3HTPMe$_3$,PFOS** and **P3HTPMe$_3$,OS**, respectively, which were determined from the onset reduction potentials.

Thermal properties

The thermal behaviour of the synthesized **P3HTPMe$_3$,X** materials was studied by rapid heat-cool calorimetry (RHC) (Fig. 1). Both a rapid cooling rate at 500 K min^{-1} and a more conventional cooling rate at 20 K min^{-1} were used. **P3HTPMe$_3$,PFOS** was found to be completely amorphous, exhibiting a glass transition (T_g) at about 95 °C. We note that this material remained fully amorphous when the cooling rate was lowered to 20 K min^{-1}. In contrast, we have reported in a previous study that **P3HTPMe$_3$,DS** exhibits semicrystalline behaviour,[21] with a T_g at about 70 °C, followed by cold crystallization when cooled at 500 K min^{-1}. The enthalpic value of the cold crystallization equals that of the subsequent melting endotherm, proving the fully amorphous nature of this material after a 500 K min^{-1} cooling. After cooling at 20 K min^{-1}, a clear double melting peak was observed with maxima at 152 and 176 °C and a combined melting enthalpy (ΔH_m) of 18.9 J g^{-1}. **P3HTPMe$_3$,OS** is also a semicrystalline material, with a higher degree of crystallinity as a higher melting enthalpy was observed and no T_g could be detected. As in **P3HTPMe$_3$,DS**, a double melting peak is observed after 20 K min^{-1} cooling, with maxima at 179 and 220 °C, yielding a total ΔH_m of 26.7 J g^{-1}. The melting peak at 179 °C can be clearly seen even after 500 K min^{-1} cooling, indicating that **P3HTPMe$_3$,OS** crystallizes more rapidly than **P3HTPMe$_3$,DS**. It seems that the materials with chemically similar DS and OS counterions show comparable behaviours, with the OS counterion leading to a higher crystallization rate and a more crystalline material. If the aliphatic chains in the OS counterion are fully fluorinated, the distorted *trans* conformation of the PFOS counterion seemingly prevents crystallization and leads to the completely amorphous **P3HTPMe$_3$,PFOS** material.

Microstructural organization in the thin polymer films

GIWAXS was used to probe the role of the counterion on the microstructural organization of thin films of **P3HTPMe$_3$** and **P3HTPMe$_3$,X**. Information on the relative crystallinity, polymer orientation and coherence length in thin films is straightforward to extract from 2D GIWAXS scattering patterns via the area, position and FWHM of the diffraction peaks.[58] X-rays are applied at an incident angle (α_i) above the critical angle (α_c) of the polymer films

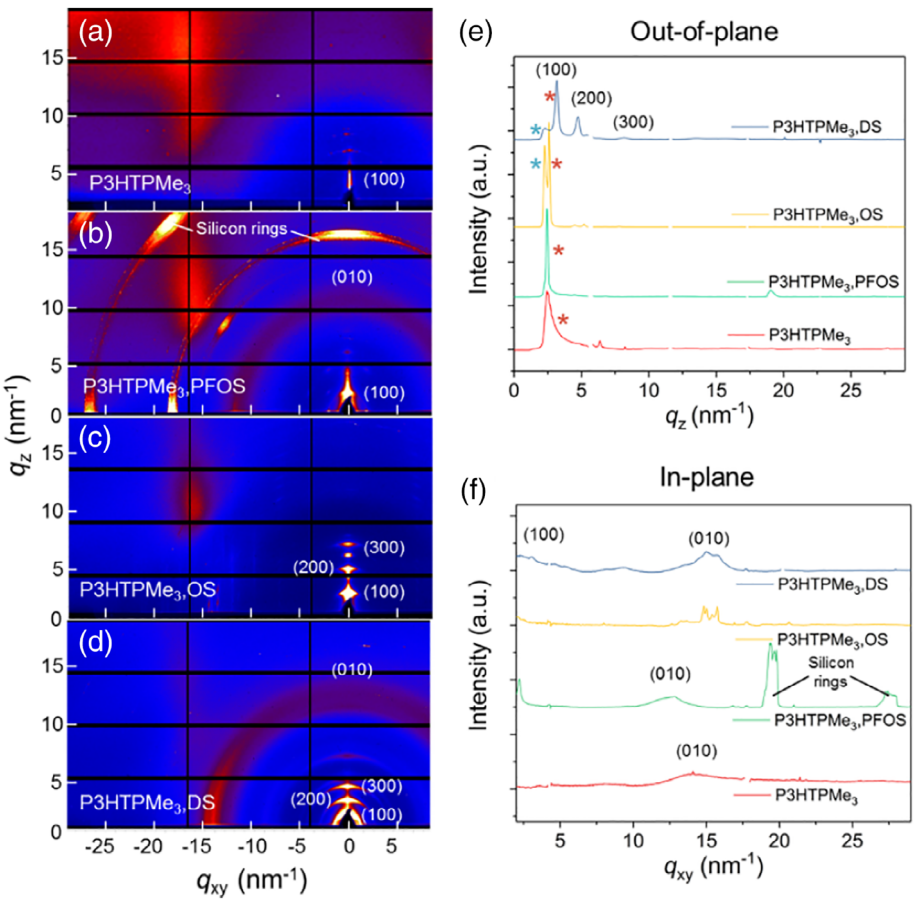

Figure 2. 2D GIWAXS scattering profiles of (a) **P3HTPMe$_3$**, (b) **P3HTPMe$_3$,PFOS**, (c) **P3HTPMe$_3$,OS** and (d) **P3HTPMe$_3$,DS** spin-coated from methanol (10 mg mL^{-1}) onto silicon wafers. Strong intensities in (b) are due to parasitic scattering from the silicon substrate. (e) Out-of-plane and (f) in-plane 1D GIWAXS line profiles corresponding to **P3HTPMe$_3$** (red line), **P3HTPMe$_3$,PFOS** (green line), **P3HTPMe$_3$,OS** (yellow line) and **P3HTPMe$_3$,DS** (blue line). Blue and red stars in (e) serve to highlight the two sets of (100) peaks in the out-of-plane profiles of **P3HTPMe$_3$,O**S and **P3HTPMe$_3$,DS**.

(a)

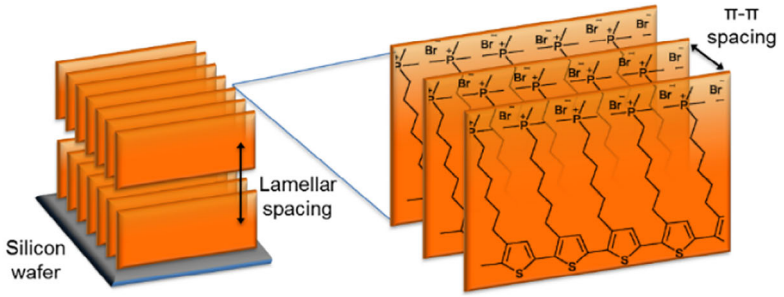

(b)

	Lamellar spacing (nm) [a]	π-π spacing (nm) [a]	Disorder parameter *g* (%) [b]
P3HTPMe$_3$	2.56	0.47	20.0
P3HTPMe$_3$,PFOS	2.51	0.52	18.9
P3HTPMe$_3$,OS	2.42, 2.86*	0.42	19.1
P3HTPMe$_3$,DS	2.51, 2.73*	0.41	13.9

[a] Lamellar and π-π spacings, *d*, were calculated from the position of the (100) and (010) peaks, *q*, respectively, using $d = 2\pi/q$. [b] Disorder parameter, *g*, was estimated using Equation 1. * The second lamellar spacings were determined from the second set of (100) peaks referred to in the text.

Figure 3. (a) Schematic representation of the edge-on alignment of polythiophene chains on a silicon wafer. (b) Table summarizing the structural information for the **P3HTPMe$_3$** and **P3HTPMe$_3$,X** (X ≡ OS, DS, PFOS) CPEs bearing different counterions obtained from GIWAXS studies.

(*ca* 0.13°) and the silicon substrate (*ca* 0.18°) to penetrate the entire thickness of the polymer film (*ca* 70–80 nm), as well as a portion of the silicon substrate, to allow for better contrast of the diffraction features while suppressing the effect of the reflected spot. Critical angles were calculated from the material scattering length densities (see the Supporting information). Figures 2(a)–2(d) show the GIWAXS patterns for pristine **P3HTPMe$_3$**, **P3HTPMe$_3$,OS**, **P3HTPMe$_3$,PFOS** and **P3HTPMe$_3$,DS** films. The 2D GIWAXS patterns for all four samples exhibit distinct lamellar packing diffractions (denoted (*h*00)) in the out-of-plane direction.[59] This crystal spacing suggests that the **P3HTPMe$_3$,X** CPE chains predominantly stack edge-on to the silicon substrate (Fig. 3).[59] The corresponding line cuts along the out-of-plane (q_z, perpendicular to the substrate) and in-plane (q_{xy}, parallel to the substrate) directions, are shown in Figs 2(e), 2(f), respectively.

For the pristine polymer **P3HTPMe$_3$** (Fig. 2(a)), an intense (100) reflection centred at $q_z = 2.5$ nm^{-1} is observed. This correlates to a lamellar spacing between the CPE backbones and across the alkyl side chains of 2.56 nm (see Fig. 3(a)), which is significantly larger than the crystal spacing of poly(3-hexylthiophene) (P3HT) (1.64 nm).[60] A weak, broad reflection is also observed along the in-plane direction at $q_{xy} \approx 13.5$ nm^{-1} (denoted (010)). This peak results from π–π stacking between the CPE backbones and corresponds to a π–π distance of 0.47 nm. The position of the original (100) peaks in the out-of-plane direction of pristine **P3HTPMe$_3$** alters slightly upon exchange of the bromide counterions with PFOS, OS and DS, resulting in reduced lamellar spacings of 2.51, 2.42 and 2.51 nm, respectively (highlighted with red asterisks in Fig. 2(e)). However, the CPEs with hydrogenated counterions also exhibit a second set of (*h*00) peaks in the out-of-plane direction at slightly lower *q* (highlighted with blue asterisks in Fig. 2(e)). These peaks correspond to larger lamellar spacings of 2.86 and 2.73 nm for **P3HTPMe$_3$,OS** and **P3HTPMe$_3$,DS**, respectively. Furthermore, the (100) peak for **P3HTPMe$_3$,DS** extends into the in-plane direction (ring peak in Fig. 2(d)). This suggests the coexistence of both edge-on and face-on orientations and may explain why two distinctive lamellar stacking peaks (blue and red asterisks) are observed for this compound. The position of the (010) peaks in the in-plane direction, and thus the π–π stacking distances, change slightly for **P3HTPMe$_3$,OS** and **P3HTPMe$_3$,DS** to 0.42 and 0.41 nm, respectively. In contrast, the π–π stacking distance in **P3HTPMe$_3$,PFOS** increases to 0.52 nm, and thus PFOS is the only counterion to cause a reduction in packing of the CPE chains.

The extent of preferential orientation in the CPE films was further investigated by performing radial and azimuthal integrations of the 2D GIWAXS scattering patterns, as shown in Fig. S10. The azimuthal integrations for each of the CPEs around $q_{xy} = 0$ nm^{-1} show narrow peaks at −90°, which highlight the preferential orientation of the CPEs in the out-of-plane direction. The widths of these bands, and therefore the preferential orientation, decrease in the order **P3HTPMe$_3$** > **P3HTPMe$_3$,OS** > **P3HTPMe$_3$,PFOS** >> **P3HTPMe$_3$,DS**. The lack of orientation in the **P3HTPMe$_3$,DS** film is clearly shown by the extremely diffuse peaks in the azimuthal integration.

The broadening of the diffraction peaks provides further information about the nature of the ordered regions within the **P3HTPMe$_3$,X** films. Peak broadening occurs due to fluctuation of the lattice spacing about a mean value, the so-called paracrystalline disorder.[61] The paracrystallinity disorder parameter *g* can be determined from the in-plane π–π stacking reflections using[61]

$$g = \sqrt{\frac{\Delta q}{2\pi q_o}} \quad (1)$$

Table 1. *J–V* parameters for PCDTBT:$PC_{71}BM$-based BHJ PSCs employing either Ca or CPE interlayers

Interfacial material	Concentration (mg mL^{-1})	V_{oc} (V)	J_{sc} (mA cm^{-2})	FF	Average η (%)[a]	Best η (%)
Ca	(30 nm)	0.84	8.61 ± 0.37	0.56	4.08 ± 0.37	4.29
$P3HTPMe_3$,PFOS	0.25	0.84	8.45 ± 0.27	0.59	4.21 ± 0.12	4.32
$P3HTPMe_3$,PFOS	**0.5**	**0.87**	**9.07 ± 0.23**	**0.60**	**4.73 ± 0.11**	**4.98**
$P3HTPMe_3$,PFOS	1	0.85	8.00 ± 0.43	0.36	2.42 ± 0.09	2.58
$P3HTPMe_3$,OS	**0.25**	**0.85**	**9.05 ± 0.33**	**0.61**	**4.70 ± 0.25**	**5.03**
$P3HTPMe_3$,OS	0.5	0.79	8.31 ± 0.41	0.37	2.43 ± 0.23	2.76
$P3HTPMe_3$,DS	0.25	0.86	9.00 ± 0.40	0.60	4.64 ± 0.30	4.96
$P3HTPMe_3$,DS	**0.5**	**0.88**	**9.17 ± 0.32**	**0.59**	**4.75 ± 0.15**	**5.00**
$P3HTPMe_3$,DS	1	0.76	8.94 ± 0.34	0.39	2.68 ± 0.26	3.12

The optimal results per concentration for each of the CPEs are indicated in bold.
[a] Average over four to eight cells.

where Δq is the FWHM of a Bragg diffraction peak and q_0 is the peak centre. The larger the value of g is, the greater is the disorder.

The lamellar spacings, π–π stacking distances and g values for thin films of **$P3HTPMe_3$,X** are summarized in Fig. 3(b). For pure **$P3HTPMe_3$** and **$P3HTPMe_3$,OS**, the (010) peaks at $q \approx 14.0$ nm^{-1} are extremely weak and broad, giving large g values of 19%–20%, which suggest a high degree of paracrystallinity disorder. For **$P3HTPMe_3$,PFOS** the (010) peak becomes slightly more intense although the paracrystallinity remains large at $g \approx 19\%$. In contrast, **$P3HTPMe_3$,DS** is significantly more ordered with $g \approx 14\%$. However, it should be noted that even this lower value remains significantly larger than that of thermally annealed P3HT (g = 6%–8%).[29]

These results seem to contrast with those obtained above from RHC studies where **$P3HTPMe_3$,OS** exhibits a higher degree of crystallinity than **$P3HTPMe_3$,DS**. However, since the CPE thin films are prepared from MeOH solutions, whereas the CPE powders are precipitated from acetone, different solution phase structures and thus a different degree of crystallinity may be expected for the powders and thin films as applied for the RHC and GIWAXS studies, respectively. This difference in the microstructural organization of the thin films of the CPEs depending on the nature of the counterion is also reflected in the morphology of the deposited CPE films. Indeed, while the morphology of the thin film of **$P3HTPMe_3$,OS** on a silicon wafer is largely featureless, the AFM images of **$P3HTPMe_3$,PFOS** and **$P3HTPMe_3$,DS** show large globular aggregates (Fig. S11).

Preferential face-on orientation and reduced π–π distances are favourable for vertical charge transport and charge carrier mobility.[62–64] The shorter π–π stacking distances imply stronger π interactions between neighbouring CPE chains.[65] Therefore, while P3HT-like chains typically lie perpendicular to the substrate,[66,67] **$P3HTPMe_3$,DS** appears to have edge-on chains coexisting with face-on packing. In contrast, **$P3HTPMe_3$,PFOS** is seemingly amorphous in the RHC studies and has a relatively large g and significantly larger π–π stacking distance compared to the other CPE thin films.

Photovoltaic properties

The behaviour of the **$P3HTPMe_3$,X** materials as cathode interlayers was then analysed by fabricating BHJ PSCs with a conventional architecture (glass/ITO/PEDOT:PSS/PCDTBT:$PC_{71}BM$/CPE (or Ca)/Al). The chemical structures of the photoactive layer components are shown in Fig. S12. The photoactive layer was deposited from *ortho*-dichlorobenzene in a 1:4 ratio with $PC_{71}BM$, with a total concentration of 20 mg mL^{-1}. The CPE interlayers were then spin-coated directly on top of the photoactive layer from methanol solutions in various concentrations (0.25, 0.5 and 1 mg mL^{-1}) to determine at which concentration the various CPE interlayers should be deposited to produce the best device performance. As indicated in Table 1 and Fig. 4, the incorporation of the **$P3HTPMe_3$,X** interlayers led to an improvement of all the device parameters (V_{oc}, J_{sc}, FF) and thus to an increase in the PCE by *ca* 15% compared to the reference device with a calcium interlayer, in line with previous investigations on similar CPE interlayers.[21,25,47,49] Nevertheless, similar PCEs are noticed regardless of the type of counterions.

Kelvin probe experiments were performed to study the work function (W_F) changes of the metal electrode in the presence of the CPE interlayer. Due to easy oxidation of Al in the atmospheric environment, we used Ag and ITO electrodes in replacement of the Al electrodes to measure the W_F change. The results of the Kelvin probe experiments indicate that the DS and OS counterions lead to a significant decrease of the W_F of the bare Ag (5.01 eV) and ITO (5.33 eV) electrodes to 4.23 eV (Ag) and 4.78 eV (ITO) for **$P3HTPMe_3$,DS**, and 4.15 eV (Ag) and 4.54 eV (ITO) for

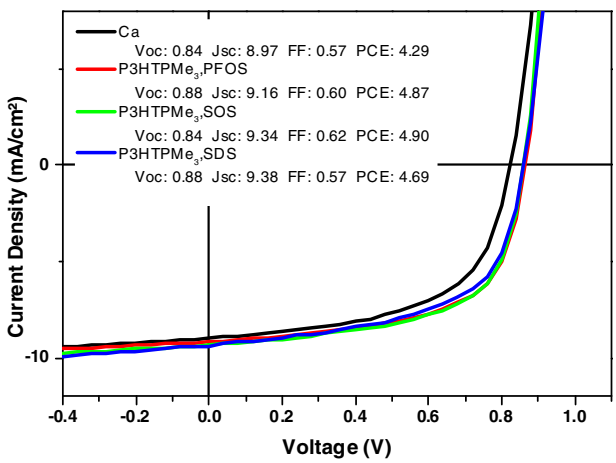

Figure 4. *J–V* curves for (average efficiency) PCDTBT:$PC_{71}BM$-based BHJ PSCs employing Ca or CPE interlayers.

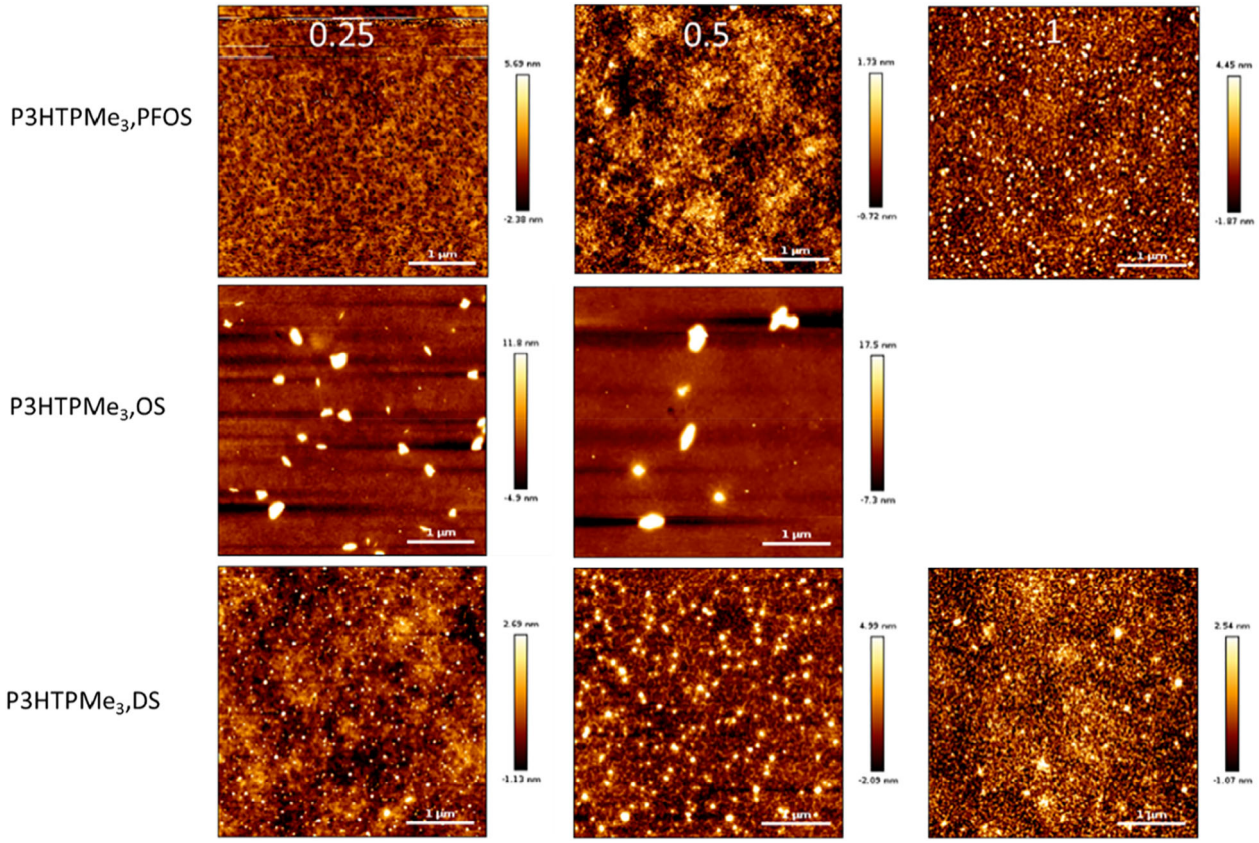

Figure 5. AFM height images (4 × 4 μm^2) of PSCs employing the **P3HTPMe$_3$,X** CPEs with different counterions for different CPE concentrations.

P3HTPMe$_3$,OS. Since it has been previously shown that CPEs lower the W_F of Ag and Al,[23,68] it is reasonable to assume that the W_F of the Al electrodes used in our solar cell devices containing either **P3HTPMe$_3$,OS** or **P3HTPMe$_3$,DS** cathode interlayers will also be lowered. In the case of **P3HTPMe$_3$,PFOS**, no clear change is observed on the W_F of the bare Ag and ITO electrodes as 5.04 eV and 5.28 eV were measured for Ag/**P3HTPMe$_3$,PFOS** and ITO/**P3HTPMe$_3$,PFOS** respectively. Since a reduced W_F of the electrodes is known to provide a better energy alignment between metal electrode and active layer which results in an enhancement of the open-circuit voltage (V_{oc}) in devices,[69,70] the weak effect of the PFOS counterion on the W_F contrasts with the increased V_{oc} noted for **P3HTPMe$_3$,PFOS**-based devices. This result may suggest that the orientation of the interfacial dipole differs according to the nature of the substrate (photoactive layer *versus* bare electrode) leading for **P3HTPMe$_3$,PFOS** to a reduced W_F when deposited on the photoactive layer, while no effect is observed when deposited on the bare electrode.

To investigate the morphology of the deposited CPE films on top of the PCDTBT:$PC_{71}BM$ active layers, AFM images were recorded for all CPE concentrations shown in Table 1. As demonstrated in Fig. 5, the **P3HTPMe$_3$,X** CPEs do not completely cover the active layer surface and they exhibit strong differences in their deposition pattern depending on the nature of the counterion. Indeed, while **P3HTPMe$_3$,DS** and **P3HTPMe$_3$,PFOS** show reasonably good affinity for deposition on top of the photoactive layer, strong 'dewetting' is observed for **P3HTPMe$_3$,OS**, with globular heights up to *ca* 20 nm. However, this improved affinity does not seem to have a major influence on the final performance, since the PCEs for all the devices are very similar. Although this observation might be somewhat surprising, it is in line with previous studies on similar polythiophene CPEs,[21,25,47,49,71] in which it was shown that it is very difficult to pinpoint specific structural requirements for CPE materials. The introduction of ionic moieties induces the formation of interfacial dipoles (i.e. capacitive double layer), enhancing charge collection while at the same time diminishing the affinity of the interlayer material for the active layer, and the increase in efficiency is dependent on the complex interplay of these two phenomena.

Finally, the stability in air of the BHJ PSCs with **P3HTPMe$_3$,X** as the interfacial layer was also investigated. New devices were prepared with the optimized CPE concentrations and these were subjected to ambient air (in the dark) for 40, 80 and 120 min. *J–V* measurements were subsequently performed in a nitrogen atmosphere to avoid additional photo-oxidation processes. As can be observed from Fig. 6 and Table S1, the reference device employing Ca as the interfacial layer degrades very quickly, with the initial PCE of 4.08% decaying rapidly to 0.55% after 40 min in air, before decreasing further to an average value of 0.13% after 2 h. This very poor device stability can be attributed to the high reactivity of Ca with oxygen.[72] Although these polythiophene-based CPEs are good alternatives to Ca as interlayer materials with respect to their electronic properties, rapid degradation of the devices may still be observed under air and moisture (if non-encapsulated) when using them as the cathode interlayer. Indeed, **P3HTPMe$_3$,OS** exhibits serious air degradation, which is even faster than observed for the Ca/Al reference device. In contrast, all other devices employing CPE interlayers

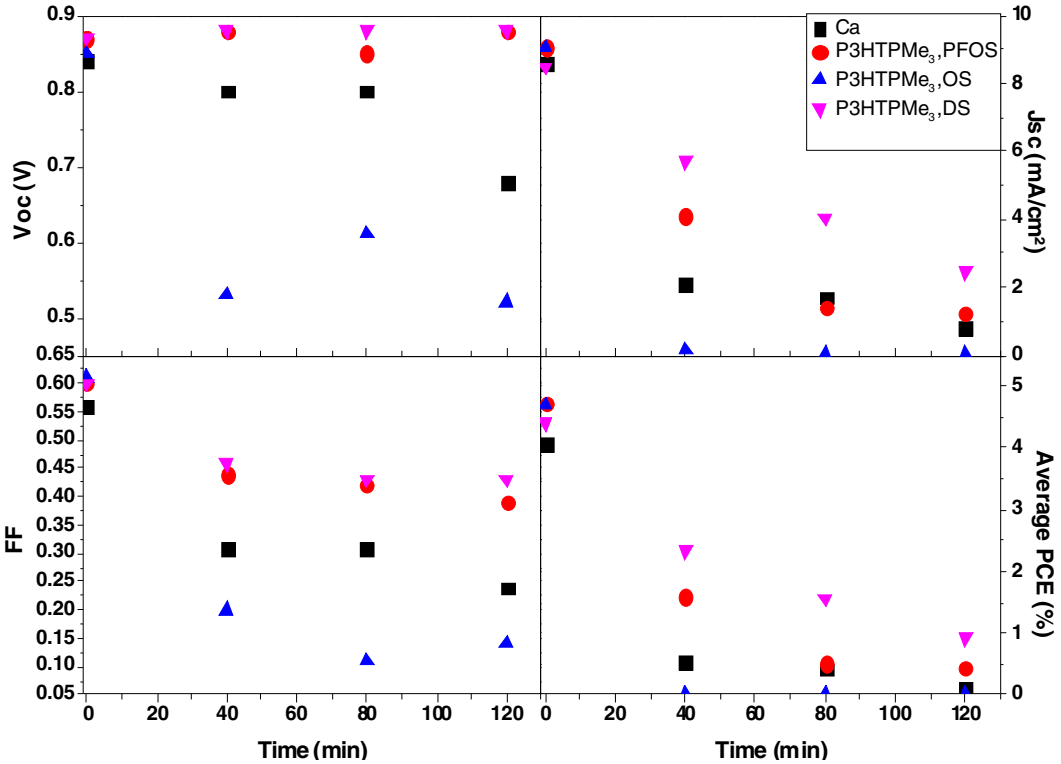

Figure 6. Degradation data (V_{oc}, J_{sc}, FF, average PCE) for PCDTBT:PC_{71}BM-based BHJ PSCs containing either Ca or **P3HTPMe$_3$,X** CPEs as the interfacial layer. The data were recorded in a nitrogen atmosphere after 0, 40, 80 and 120 min of exposure to air (in the dark).

outlast the reference device, with the best device being that based on **P3HTPMe$_3$,DS**, mainly due to a better retention of the V_{oc}. It should also be noted that the devices with the more stable FFs are those with a more complete active layer coverage (Fig. 2) (**P3HTPMe$_3$,PFOS** and **P3HTPMe$_3$,DS**), which could suggest more stable interfacial properties.

CONCLUSIONS

Three CPEs with identical polythiophene backbones and phosphonium side groups, but different charge-compensating ions, were synthesized. Changing the nature of the counterions drastically affects the glass transition temperature as well as the crystallinity of the materials. **P3HTPMe$_3$,PFOS** is completely amorphous, whereas **P3HTPMe$_3$,OS** and **P3HTPMe$_3$,DS** exhibit a semicrystalline behaviour. GIWAXS studies also indicate that the microstructural organization of thin polymer films is dependent on the nature of the counterion species. While **P3HTPMe3,DS** and **P3HTPMe$_3$,OS** exhibit shortened π–π stacking distances, the PFOS counterion causes a reduction in packing distance of the CPE chains. In addition, the coexistence of both edge-on and face-on orientations is also noticed for **P3HTPMe$_3$,DS**. Although AFM and Kelvin probe studies revealed different adhesion coverage efficiencies and work function changes depending on the nature of the counterion species, this does not lead to significant differences in their photovoltaic performance as cathode interfacial layers. To explain this behaviour, a delicate balance between a wide variety of factors such as the material's affinity with the underlying photoactive layer, the ability to create a stable capacitive double layer[47] or the molecular ordering in thin films may be considered. Finally, some of these CPE cathode interlayers lead to higher device stability in air in comparison with the reference device with a calcium interlayer, highlighting their potential for the fabrication of stable and highly performant PSCs.

ACKNOWLEDGEMENTS

This work was supported by the CNRS and the Université de Montpellier. This work was also supported in part by the Science Foundation Ireland under grant no. 12/IP/1608. Research in Mons is supported by FNRS-FRFC (2Dto3D project – EOS programme) and Région Wallonne (OPTI2MAT excellence programme). The University of Mons and Hasselt University co-authors are grateful for financial support by the Science Policy Office of the Belgian Federal Government (BELSPO; PAI/IAP 7/05). JK is a postdoctoral fellow of the Research Foundation – Flanders (FWO Vlaanderen). NVdB thanks the Vrije Universiteit Brussel for a post-doctoral grant. The HINT COST action MP1202 and French–Irish programme 'Hubert Curien Ulysses' (31998ZF) are also acknowledged for support. This research has also been supported by the European Commission under the 7th Framework Programme through the 'Research Infrastructures' action of the 'Capacities' programme (contract no. CP-CSA_INFRA-2008-1.1.1 Number 226507-NM13). We further thank the Diamond Light Source for beamtime at the I07 beamline (experiment SI13868) and TA Instruments for the RHC equipment.

SUPPORTING INFORMATION

Supporting information may be found in the online version of this article.

REFERENCES

1 Jiang H, Taranekar P, Reynolds JR and Schanze KS, *Angew Chem Int Ed* **48**:4300–4316 (2009).
2 Schanze KS and Zhao X, Structure-property relationships and applications of conjugated polyelectrolytes, in *Handbook of Conducting Polymers*, Vol. **1**, 3rd edn, ed. by Skotheim TA and Reynolds JR. CRC Press, Boca Raton, FL, pp. 14-1–14-29 (2007).
3 by Liu B and Bazan GC eds, *Conjugated Polyelectrolytes: Fundamentals and Applications*. Wiley-VCH, Weinheim (2013).
4 Liang J, Li K and Liu B, *Chem Sci* **4**:1377–1394 (2013).
5 Feng X, Liu L, Wang S and Zhu D, *Chem Soc Rev* **39**:2411–2419 (2010).
6 Das S, Routh P, Ghosh R, Chatterjee DP and Nandi AK, *Polym Int* **66**: 623–639 (2017).
7 Zhan R and Liu B, *Chem Rec* **16**:1715–1740 (2016).
8 Lee S, Jang CH, Nguyen TL, Kim SH, Lee KM, Chang K *et al.*, *Adv Mater* **31**:1900067 (2019).
9 Lee BR, Yu JC, Park JH, Lee S, Mai C-K, Zhao B *et al.*, *ACS Nano* **12**: 5826–5833 (2018).
10 Lee Y, Suh M, Kim K, Kim H, Kim D, Chang H *et al.*, *Org Electron* **43**:64–69 (2017).
11 Nishikitani Y, Inokuchi N, Nishide H, Uchida S, Shibanuma T and Nishimura S, *J Phys Chem C* **120**:13976–13986 (2016).
12 Lee W, Seo JH and Woo HY, *Polymer* **54**:5104–5121 (2013).
13 Hu Z, Zhang K, Huang F and Cao Y, *Chem Commun* **51**:5572–5585 (2015).
14 Schmode P, Ohayon D, Reichstein PM, Savva A, Inal S and Thelakkat M, *Chem Mater* **31**:5286–5295 (2019).
15 Musumeci C, Vagin M, Zeglio E, Ouyang L, Gabrielsson R and Inganäs O, *J Mater Chem C* **7**:2987–2993 (2019).
16 Zeglio E, Eriksson J, Gabrielsson R, Solin N and Inganäs O, *Adv Mater* **29**: 1605787 (2017).
17 Zeglio E, Schmidt MM, Thelakkat M, Gabrielsson R, Solin N and Inganäs O, *Chem Mater* **29**:4293–4300 (2017).
18 Zeglio E, Vagin M, Musumeci C, Ajjan FN, Gabrielsson R, Trinh XT *et al.*, *Chem Mater* **27**:6385–6393 (2015).
19 Houston JE, Richeter S, Clément S and Evans RC, *Polym Int* **66**: 1333–1348 (2017).
20 He Z, Wu H and Cao Y, *Adv Mater* **26**:1006–1024 (2014).
21 Chevrier M, Houston JE, Kesters J, Van den Brande N, Terry AE, Richeter S *et al.*, *J Mater Chem A* **3**:23905–23916 (2015).
22 Seo JH, Yang R, Brzezinski JZ, Walker B, Bazan GC and Nguyen T-Q, *Adv Mater* **21**:1006–1011 (2009).
23 van Reenen S, Kouijzer S, Janssen RAJ, Wienk MM and Kemerink M, *Adv Mater Interfaces* **1**:1400189 (2014).
24 Jo MY, Ha YE, Won YS, Yoo SI and Kim JH, *Org Electron* **25**:85–91 (2015).
25 Drijkoningen J, Kesters J, Vangerven T, Bourgeois E, Lutsen L, Vanderzande D *et al.*, *Org Electron* **15**:1282–1289 (2014).
26 Voortman TP and Chiechi RC, *ACS Appl Mater Interfaces* **7**:28006–28012 (2015).
27 Houston JE, Chevrier M, Appavou M-S, King SM, Clément S and Evans RC, *Nanoscale* **9**:17481–17493 (2017).
28 Korevaar PA, de Greef TFA and Meijer EW, *Chem Mater* **26**:576–586 (2014).
29 Noriega R, Rivnay J, Vandewal K, Koch FPV, Stingelin N, Smith P *et al.*, *Nat Mater* **12**:1038–1044 (2013).
30 Ying L, Huang F and Bazan GC, *Nat Commun* **8**:14047 (2017).
31 Hostnik G, Podlipnik Č, Mériguet G and Cerar J, *Macromolecules* **53**: 1119–1128 (2020).
32 Yang R, Garcia A, Korystov D, Mikhailovsky A, Bazan GC and Nguyen T-Q, *J Am Chem Soc* **128**:16532–16539 (2006).
33 Hostnik G, Bončina M, Dolce C, Mériguet G, Rollet A-L and Cerar J, *Phys Chem Chem Phys* **18**:25036–25047 (2016).
34 McCullough RD, Ewbank PC and Loewe RS, *J Am Chem Soc* **119**: 633–634 (1997).
35 Chen Z, Hu Z, Wu Z, Liu X, Jin Y, Xiao M *et al.*, *J Mater Chem A* **5**: 19447–19455 (2017).
36 Danesh CD, Starkweather NS and Zhang S, *J Phys Chem B* **116**: 12887–12894 (2012).
37 Burrows HD, Tapia MJ, Silva CL, Pais AACC, Fonseca SM, Pina J *et al.*, *J Phys Chem B* **111**:4401–4410 (2007).
38 Chen L, Xu S, McBranch D and Whitten D, *J Am Chem Soc* **122**: 9302–9303 (2000).
39 Evans RC, Knaapila M, Willis-Fox N, Kraft M, Terry A, Burrows HD *et al.*, *Langmuir* **28**:12348–12356 (2012).
40 Knaapila M, Evans RC, Garamus VM, Almásy L, Székely NK, Gutacker A *et al.*, *Langmuir* **26**:15634–15643 (2010).
41 Knaapila M, Evans RC, Gutacker A, Garamus VM, Székely NK, Scherf U *et al.*, *Soft Matter* **7**:6863–6872 (2011).
42 Chang Y-M, Zhu R, Richard E, Chen C-C, Li G and Yang Y, *Adv Funct Mater* **22**:3284–3289 (2012).
43 Garcia A, Jin Y, Brzezinski JZ and Nguyen T-Q, *J Phys Chem C* **114**: 22309–22315 (2010).
44 Schmidt MM, ElMahmoudy M, Malliaras GG, Inal S and Thelakkat M, *Macromol Chem Phys* **219**:1700374 (2018).
45 Garcia A, Brzezinski JZ and Nguyen T-Q, *J Phys Chem C* **113**:2950–2954 (2009).
46 Do TT, Hong HS, Ha YE, Park J, Kang Y-C and Kim JH, *ACS Appl Mater Interfaces* **7**:3335–3341 (2015).
47 Kesters J, Govaerts S, Pirotte G, Drijkoningen J, Chevrier M, Van den Brande N *et al.*, *ACS Appl Mater Interfaces* **8**:6309–6314 (2016).
48 Seo JH, Gutacker A, Sun Y, Wu H, Huang F, Cao Y *et al.*, *J Am Chem Soc* **133**:8416–8419 (2011).
49 Kesters J, Ghoos T, Penxten H, Drijkoningen J, Vangerven T, Lyons DM *et al.*, *Adv Energy Mater* **3**:1180–1185 (2013).
50 Rubio-Magnieto J, Thomas A, Richeter S, Mehdi A, Dubois P, Lazzaroni R *et al.*, *Chem Commun* **49**:5483–5485 (2013).
51 Scofield JH, *J Electron Spectrosc Relat Phenom* **8**:129–137 (1976).
52 Wouters S, Demir F, Beenaerts L and Van Assche G, *Thermochim Acta* **530**:64–72 (2012).
53 Bard AJ and Faulker LR, *Electrochemical Methods: Fundamentals and Applications*, 2nd edn. John Wiley and Sons, New York (2001).
54 Trasatti S, *Pure Appl Chem* **58**:955–966 (1986).
55 Danley RL, Caulfield PA and Aubuchon SR, *Am Lab* **40**:9–11 (2008).
56 Nicklin C, Arnold T, Rawle J and Warne A, *J Synchrotron Radiat* **23**: 1245–1253 (2016).
57 Basham M, Filik J, Wharmby MT, Chang PCY, El Kassaby B, Gerring M *et al.*, *J Synchrotron Radiat* **22**:853–858 (2015).
58 Rivnay J, Mannsfeld SCB, Miller CE, Salleo A and Toney MF, *Chem Rev* **112**:5488–5519 (2012).
59 Sirringhaus H, Brown PJ, Friend RH, Nielsen MM, Bechgaard K, Langeveld-Voss BMW *et al.*, *Nature* **401**:685–688 (1999).
60 Chen T-A, Wu X and Rieke RD, *J Am Chem Soc* **117**:233–244 (1995).
61 Hindeleh AM and Hosemann R, *J Phys C* **21**:4155–4170 (1988).
62 Guo J, Liang Y, Szarko J, Lee B, Son HJ, Rolczynski BS *et al.*, *J Phys Chem B* **114**:742–748 (2010).
63 Jung J, Lee W, Lee C, Ahn H and Kim BJ, *Adv Energy Mater* **6**:1600504 (2016).
64 Lei T, Dou J-H and Pei J, *Adv Mater* **24**:6457–6461 (2012).
65 Nguyen TL, Choi H, Ko SJ, Uddin MA, Walker B, Yum S *et al.*, *Energy Environ Sci* **7**:3040–3051 (2014).
66 Park YD, Lee HS, Choi YJ, Kwak D, Cho JH, Lee S *et al.*, *Adv Funct Mater* **19**:1200–1206 (2009).
67 Kim BJ, Miyamoto Y, Ma B and Fréchet JMJ, *Adv Funct Mater* **19**: 2273–2281 (2009).
68 Zhou Y, Fuentes-Hernandez C, Shim J, Meyer J, Giordano AJ, Li H *et al.*, *Science* **336**:327–332 (2012).
69 Hu Z, Zheng N, Dong S, Liu X, Chen Z, Ying L *et al.*, *Org Electron* **57**: 151–157 (2018).
70 Zhang K, Zhong C, Liu S, Mu C, Li Z, Yan H *et al.*, *ACS Appl Mater Interfaces* **6**:10429–10435 (2014).
71 Govaerts S, Kesters J, Defour M, Van Mele B, Penxten H, Neupane S *et al.*, *Eur Polym J* **97**:49–56 (2017).
72 Jørgensen M, Norrman K and Krebs FC, *Sol Energy Mater Sol Cells* **92**: 686–714 (2008).

